The Astrophysical Journal, 977:107 (15pp), 2024 December 10 https://doi.org/10.3847/1538-4357/ad7a00

The Lyα Dependence on Nebular Properties from the HETDEX and MOSDEF Surveys

Óscar A. Chávez Ortiz[1,10], Gene C. K. Leung[1], Steven L. Finkelstein[1], Dustin Davis[1], Ralph S. Sutherland[2], David C. Nicholls[2], Mabel Stephenson[1], Erin Mentuch Cooper[1], Micaela Bagley[1], Karl Gebhardt[1], Lindsay R. House[1,11], Chenxu Liu[1,3], Robin Ciardullo[4,5], Caryl Gronwall[4,5], Gary J. Hill[6,7], Daniel Farrow[8,9], and Donald P. Schneider[4,5]

[1] Department of Astronomy, The University of Texas at Austin, 2515 Speedway Boulevard, Austin, TX 78712, USA
[2] Research School of Astronomy and Astrophysics, Australian National University, Canberra, ACT, Australia
[3] South-Western Institute for Astronomy Research, Yunnan University, Kunming, Yunnan 650500, People's Republic of China
[4] Department of Astronomy & Astrophysics, The Pennsylvania State University, University Park, PA 16802, USA
[5] Institute for Gravitation and the Cosmos, The Pennsylvania State University, University Park, PA 16802, USA
[6] McDonald Observatory, The University of Texas at Austin, 2515 Speedway Boulevard, Stop C1402, Austin, TX 78712, USA
[7] Department of Astronomy, The University of Texas at Austin, 2515 Speedway Boulevard, Stop C1400, Austin, TX 78712, USA
[8] Centre of Excellence for AI, Data Science and Modeling (DAIM), University of Hull, Cottingham Road, Hull, HU6 7RX, UK
[9] E. A. Milne Centre for Astrophysics, University of Hull, Cottingham Road, Hull, HU6 7RX, UK

Received 2024 April 1; revised 2024 August 27; accepted 2024 September 10; published 2024 December 5

Abstract

Investigating the impact of galaxy properties on emergent Lyα emission is crucial for reionization studies, given the sensitivity of Lyα to neutral hydrogen. This study presents an analysis of the physical characteristics of 155 star-forming galaxies, 29 with Lyα detected, and 126 with Lyα not detected with Lyα EW < 20 Å, at $z = 1.9$–3.5, drawn from the MOSFIRE Deep Evolution Field survey, that have overlapping observations from the Hobby–Eberly Telescope Dark Energy Experiment survey. To unravel the interstellar medium (ISM) conditions in our sample, we developed a custom nebular line modeling algorithm based on the MAPPINGS V photoionization model grid and the `emcee` framework. Combining nebular-based ISM properties with photometry-based global properties, constrained via `Bagpipes`, we explore distinctions in the stellar and gas properties between Lyα-detected and Lyα-nondetected galaxies. Our analysis reveals statistically significant differences between the two samples in terms of stellar mass and dust attenuation (A_V) at $>2\sigma$ significance, as determined via a Kolmogorov–Smirnov test. Moreover, there are weaker ($\lesssim 1\sigma$ significance) indications that the ionization parameter and metallicity differ between the two samples. Our results demonstrate that the escape fraction of Lyα ($f_{\rm esc}^{\rm Ly\alpha}$) is inversely correlated with stellar mass, star formation rate, and dust attenuation, while it is positively correlated with the ionization parameter, with significance levels exceeding 2σ. Our findings suggest that the interstellar environments of Lyα-detected galaxies, characterized by low mass, low dust, low gas-phase metallicity, and high ionization parameters, play a pivotal role in promoting the escape of Lyα radiation.

Unified Astronomy Thesaurus concepts: Galaxies (573); Lyα galaxies (978); Galaxy properties (615)

1. Introduction

The epoch of reionization marks the last major phase transition that the intergalactic medium (IGM) has undergone (X. Fan et al. 2006; B. E. Robertson et al. 2015; S. Finkelstein et al. 2019). The evolution of the IGM encodes the dominant ionizing sources that were responsible for driving reionization. Current reionization models diverge between predicting an early reionization history, dominated by low-mass galaxies (S. L. Finkelstein et al. 2019), or a late reionization history, dominated by high-mass systems (B. E. Robertson et al. 2015). The reionization timeline can be quantified by measuring the neutral hydrogen content as a function of redshift during the epoch of reionization. A useful tracer that is highly sensitive to the surrounding neutral hydrogen content and can be used throughout the epoch of reionization is the Lyα emission line. Due to its large interaction cross-section, Lyα is able to easily scatter from our line of sight due to the presence of intervening neutral hydrogen (J. E. Gunn & B. A. Peterson 1965; J. Miralda-Escudé 1998; S. Malhotra & J. E. Rhoads 2006; M. Dijkstra 2014). Comparing the ratio of the observed Lyα flux to the intrinsic Lyα production of a galaxy enables the measurement of the neutral fraction near the galaxy. However, determining the intrinsic production of Lyα from galaxies at high redshift has proven to be difficult. Other galaxy properties, such as dust and galaxy kinematics, drastically alter the amount of Lyα emission that escapes a galaxy and subsequently interacts with the IGM (A. Verhamme et al. 2006, 2008; M. Dijkstra 2014). An in-depth analysis of the properties that regulate the amount of Lyα escape is needed to understand the mechanism(s) promoting or hindering Lyα observability. This direct link between galaxy properties and its effect on Lyα emission can best be accomplished via spectroscopic analysis through the use of nebular lines to directly probe galactic averaged interstellar medium (ISM) conditions.

The nebular emission lines hold a wealth of information about the physical conditions within the ISM of galaxies. Emission lines reveal episodes of recent star formation activity by converting the emission line luminosity to a star formation rate (SFR), using relations from R. C. Kennicutt (1998) and R. C. Kennicutt & N. J. Evans (2012). Emission lines can also be used to study the radiation field of galaxies through a set of

---

[10] NASA FINESST Fellow.
[11] NSF Graduate Research Fellow.

line ratio diagnostics (G. Kauffmann et al. 2003; L. J. Kewley et al. 2006), indicating if the radiation is predominantly powered through star formation or an active galactic nucleus (AGN). Emission lines of hydrogen, mainly through the ratio of $\mathrm{H}\alpha/\mathrm{H}\beta$, have the ability to provide constraining information about the dust within the galaxy through the Balmer decrement (see R. C. Kennicutt 1992; J. Brinchmann et al. 2004; A. Domínguez et al. 2013). As such, nebular lines hold the key to understanding crucial ISM conditions that can ultimately affect Lyα escape.

To date, two key methods are employed in the analysis of emission lines to determine the physical properties of galaxies. The first method involves comparing observed emission line data to empirically derived relations, yielding insights into quantities like metallicity (L. J. Kewley & S. L. Ellison 2008; R. L. Sanders et al. 2021; D. Langeroodi et al. 2023; I. H. Laseter et al. 2024), SFR (T. Fetherolf et al. 2021; K. Nakajima et al. 2023; A. E. Shapley et al. 2023), and ionization parameters (R. Bassett et al. 2019; N. Kumari et al. 2021). However, these empirical calibrations may lose accuracy when applied to higher-redshift galaxies, where the scaling relations derived at lower redshift may not be applicable (see J. S. Brown et al. 2016; L. L. Cowie et al. 2016; F. Bian et al. 2018).

The second method involves comparing measured emission line fluxes and ratios against theoretical models that incorporate up-to-date atomic physics and high-precision atomic data. State-of-the-art codes such as MAPPINGS V and `Cloudy` provide exceptional flexibility, allowing the simulation of observed fluxes based on a set of defined input parameters, as demonstrated by R. S. Sutherland & M. A. Dopita (2017) and Ferland (2017). This approach enables us to dissect the impact that various parameters have on the model, ultimately deepening our comprehension of the ISM's pivotal role in governing the radiative transfer of observed emission lines and their ties to Lyα escape.

Studying the internal properties of galaxies with and without Lyα emission holds the potential to unveil critical determinants of Lyα escape. Previous research on Lyα emitters (LAEs) have uncovered overarching trends linked to global galaxy properties and the intensity of Lyα emission through observation (see A. E. Shapley et al. 2003; L. Guaita et al. 2011; J. Matthee et al. 2016; R. F. Trainor et al. 2016; X. Du et al. 2021; R. Pucha et al. 2022; Z. Chen et al. 2024; L. Napolitano et al. 2024) and theory (see P. Laursen et al. 2009; H. Yajima et al. 2014). Our endeavor seeks to expand upon this body of work by exploring both Lyα emitting and nonemitting galaxies under the same methodology, with the objective of deciphering the underlying drivers of these trends within the subset of galaxies characterized by Lyα emission.

Furthermore, the data set for this analysis is required to minimize the Lyα attenuation by the IGM. Such conditions are typically met at $z \lesssim 5.5$, as the IGM is predominantly ionized in this regime (X. Fan et al. 2006). It is only through the availability of such a data set that we can effectively discern the potential galaxy properties contributing to the facilitation of Lyα escape, if they indeed exist.

Numerous surveys in the scientific literature have undertaken the acquisition of deep spectra for galaxies at $z < 5$, followed by subsequent observations to acquire the Lyman continuum and Lyα properties (see X. Du et al. 2021). Among the comprehensive array of studies, one that stands out is the MOSFIRE Deep Evolution Field (MOSDEF) survey (M. Kriek et al. 2015; N. A. Reddy et al. 2015). MOSDEF is a spectroscopic survey that has obtained near-infrared spectra for over 1000 galaxies, spanning the redshift range of 1.5–4.5 in the Cosmic Assembly Near-infrared Deep Extragalactic Legacy Survey (CANDELS) fields (N. A. Grogin et al. 2011). To carry out our investigations, we incorporate Lyα spectroscopic data gathered by the Hobby–Eberly Telescope Dark Energy Experiment (HETDEX). HETDEX has observed four of the five CANDELS fields and can detect Lyα emission from galaxies within the redshift range of 1.9–3.5 (K. Gebhardt et al. 2021; G. J. Hill et al. 2021; E. Mentuch Cooper et al. 2023). These two data sets are vital to discern and characterize the disparities between galaxies exhibiting Lyα emission and those that do not.

The paper is structured as follows, Section 2 covers the data products used in the paper, Section 3 describes our methodology, Section 4 presents the results of our analysis, Section 5 covers a discussion of the results and their implications, and Section 6 summarizes our results and presents concluding remarks.

We assume a cosmological model with $H_0 = 70\ \mathrm{km\ s^{-1}\ Mpc^{-1}}$, $\Omega_{m,0} = 0.3$, and $\Omega_{\Lambda,0} = 0.7$, and all magnitudes reported are expressed in the AB magnitude system (J. B. Oke 1974; J. B. Oke & J. E. Gunn 1983).

2. Data

Our study uses data from two surveys to investigate the impact that galaxy properties have on Lyα visibility through rest-frame optical and UV spectra. For the rest-frame optical regime, we use the publicly available MOSDEF (M. Kriek et al. 2015) near-infrared spectroscopic survey, encompassing roughly 1500 galaxies at $z = 1$–4. These galaxies have been selected using H-band magnitude criteria, with varying thresholds across the CANDELS fields, and have a wealth of ancillary photometric data enabling a robust assessment of global galaxy properties through spectral energy distribution (SED) fitting. To explore the rest-frame UV, in particular the Lyα detections, we turn to the optical spectra provided by the HETDEX survey (K. Gebhardt et al. 2021), which observed four of the five CANDELS fields. Integrating these two surveys, we cross-reference sources from MOSDEF with the HETDEX database, allowing the creation of two sample populations: galaxies with detected Lyα and those without. This approach enables us to discern the impact of galaxy properties on Lyα detection.

2.1. Rest-frame UV Spectroscopic Data

On the Hobby–Eberly Telescope (HET; L. W. Ramsey et al. 1998) resides the Visible Integral-field Replicable Unit Spectrograph (VIRUS; G. J. Hill et al. 2021), a wide-field, fiber integral field unit (IFU) spectrograph with 78 total IFUs feeding 156 spectrographs, and a spectroscopic resolution ranging from 4.7 to 5.6 Å (resolving power of 750–950; G. J. Hill et al. 2021). VIRUS has a wavelength coverage of 3500–5500 Å, which is sensitive to Lyα at $1.9 < z < 3.5$. Each IFU has 51×51 sq.$''$ area with 448 $1\farcs5$-diameter fibers, which have a $1/3$ filling factor. The standard HETDEX observational strategy employs three small offsets (dithers) to fill the interfiber gaps, yielding fully filled IFUs. The total area covered for a fully filled IFU "shot" is roughly $18' \times 18'$ at a $1/4.5$ filling factor (accounting for the inter-IFU gaps and a central hole, where the remaining HET instrument feeds are located).

The processing of the data uses the HETDEX data reduction pipeline, which (1) reduces and calibrates the spectroscopic data, (2) finds emission line(s) in the spectrum, and (3) attempts to classify any line it detects, largely based on the approach from A. S. Leung et al. (2017), in an automated emission line classification scheme called ELiXer (D. J. Farrow et al. 2021; K. Gebhardt et al. 2021; D. Davis et al. 2023a). This results in a fully flux-calibrated, PSF-weighted spectrum. We refer the reader to K. Gebhardt et al. (2021) for the full methodology for data reduction, line extraction, and detection implemented by the HETDEX reduction pipeline. Every flux-calibrated spectrum is stored and cataloged in the internal HETDEX database.

In this study, we utilize the most current internal data release, denoted as HETDEX Data Release 3 (HDR3), which includes an emission line detection catalog. This catalog contains essential information pertaining to the detected sources, encompassing spatial coordinates, line flux measurements, full width at half maximum values, and spectroscopic redshift determinations. HDR3 represents a substantial advancement over its predecessor, the publicly accessible catalog HDR2 (E. Mentuch Cooper et al. 2023), marked by its implementation of better noise modeling, quality assessment flags, and an expanded survey area. HETDEX is a flux-limited survey, sensitive at detecting Lyα flux of 4×10^{-17} erg s^{-1} cm^{-2} (5σ) above redshift 2.5, with the sensitivity being 30% higher around redshift 2. We note that, due to the HETDEX flux limit, there may be a set of MOSDEF galaxies with faint Lyα emission that HETDEX will not be as sensitive to.

2.2. MOSDEF Spectroscopic Data

MOSDEF is a rest-frame optical spectroscopic survey of approximately 1500 galaxies distributed across the redshift range of 1.37–3.8. These galaxies have rest-frame optical spectra in the Y, J, H, and K bands measured using the MOSFIRE instrument on the Keck Observatory in Hawaii (I. S. McLean et al. 2012; M. Kriek et al. 2015). The selection process for the MOSDEF sources adhere to an H-band magnitude criterion, with discrete thresholds set at $H = 24.0$, $H = 24.5$, and $H = 25.0$, aptly tailored to yield a consistent stellar mass limit of $10^9\,M_\odot$ across redshifts $1.37 \leqslant z \leqslant 1.7$, $2.09 \leqslant z \leqslant 2.61$, and $2.95 \leqslant z \leqslant 3.8$, respectively, across the CANDELS fields. The MOSDEF galaxy sample covers a broad range of galaxies with many different galaxy properties, allowing the determination of the physical properties that lead to enhancement in Lyα detection.

The MOSDEF spectra undergo a comprehensive reduction process, as described by M. Kriek et al. (2015) and N. A. Reddy et al. (2015), encompassing corrections for both slit-loss and underlying stellar absorption features via stellar population modeling. The aforementioned references also detail the procedures employed for emission line fitting, with the resulting flux measurements accessible within the publicly available catalog named *linemeas_cor.fits* on the MOSDEF website, housing the rest-frame optical line flux data from these galaxies. The catalog includes spectroscopic redshift values determined through emission line fitting for 74% of the total MOSDEF sources. In cases where multiple emission lines contribute to redshift determinations, the catalog assigns the highest quality assurance flag, *Z_QUAL=7*. In situations where a single emission line is available, corroborating data sources, including previous spectroscopic redshifts from another survey, the highest probability density acquired by the photometric redshift distributions, and when necessary, validation via visual inspection, are used to assess the quality of the redshift.

2.3. Photometric Data

The photometric data used in this analysis is from the CANDELS survey (N. A. Grogin et al. 2011; A. M. Koekemoer et al. 2011), which includes ACS optical and WFC3 near-infrared imaging from the Hubble Space Telescope (HST). We use the measurements from the 3D-HST photometric catalogs in the four fields that have HETDEX coverage: AEGIS, COSMOS, GOODS-N, and UDS. We refer the readers to R. E. Skelton et al. (2014) and G. B. Brammer et al. (2012) for further information on the photometric data and measurements. The large number of photometric bands, >10 in most cases, is crucial to constrain the SED of galaxies to obtain robust measurements of the galaxy's global physical properties. We crossed matched the `MOSDEF` sources via their coordinates and required a separation of <0.05" to ensure a proper match to the photometric information that we used in our SED analysis in Section 3.

2.4. Sample Selection

Our principal scientific objective revolves around understanding what physical properties are different in an H-band magnitude selected sample between galaxies exhibiting detectable Lyα emission and those without. To accomplish this goal, we cross-match the MOSDEF emission-line catalog with sources in the internal data release HDR3, using a search radius of 1″. This choice aligns with previous findings by A. P. McCarron et al. (2022), indicating that the majority of HETDEX detections have imaging counterparts within this search radius. To increase the confidence of a counterpart match, we redshifted the rest-frame Lyα line at 1215.67 Å using the MOSDEF spectroscopic redshift information and verified that the observed wavelength, as reported by HETDEX, coincides with the expected position of the Lyα line. Given the well-documented Lyα velocity offsets associated with gas kinematics (M. Dijkstra 2014), we established a search window of ± 500 km s^{-1}, encompassing both moderate and extreme Lyα velocity offsets, in accordance with the observations of R. Endsley et al. (2022). Sources that successfully satisfied both the spatial and spectral criteria were deemed matches and were incorporated into our Lyα-detected sample.

In cases where a match between `MOSDEF` sources and the HDR3 detections catalog was not found, we initiated an independent search for Lyα lines, aiming to accommodate detections with lower line fluxes when feasible and establish stringent upper limits on the line flux when no detection was achieved. This independent search procedure entailed the extraction of a HETDEX spectrum at the coordinates of the MOSDEF source, followed by an attempt to fit a Gaussian line profile model at $1215.67 \times (1 + z_{\rm mosfire})$ within a ± 500 km s^{-1} velocity offset window using `emcee`. The model fit quality was assessed by ensuring that the reduced chi-squared (χ^2) value approached unity and by cross-checking against other Gaussian fits across the spectrum. We fit a Gaussian profile using `emcee` to regions of the spectrum without Lyα and computed the signal-to-noise ratio (SNR) of those non-Lyα fits to determine if noise can mimic a real detection. We define SNR as the median flux divided by the average of the absolute differences between the median value and the 16th and 84th percentiles from the line flux posterior derived from the `emcee` line-fitting runs. We checked the distribution of SNR from the non-Lyα fits against the SNR from the Lyα fit and found that in all cases there were non-Lyα fits that matched or exceeded the SNR of our Lyα fit, indicating that noise could mimic a real detection. As a result, we do not add any lines identified from our own line search into the Lyα-detected sample.

At this stage, our data set comprised a total of 502 MOSDEF sources, among which 42 exhibited detectable Lyα emission as observed by HETDEX in the HDR3 catalog. As an additional refinement, we screened our data set for the presence of potential AGNs, using results from prior efforts in identifying and analyzing AGNs within the MOSDEF survey (see G. C. K. Leung et al. 2019), as well as AGN investigations in the HETDEX data set (see C. Liu et al. 2022). We cross-referenced the AGN catalog from G. C. K. Leung et al. (2019) with our data set, excluding all sources bearing AGNFLAG designations of 1–5, indicative of detectable X-ray and/or infrared AGN signatures, or sources positioned above the L. J. Kewley et al. (2013) line at $z \approx 2.3$ and beyond the G. Kauffmann et al. (2003) demarcation in the BPT diagram.

We also cross-matched our Lyα-detected sources with the AGN catalog in C. Liu et al. (2022) to ensure a comprehensive AGN exclusion process. This AGN filtering resulted in the removal of an additional 56 sources from the sample of 502 sources, where 8 of the 56 removed were initially identified within our Lyα-detected sample, ultimately culminating in a refined data set consisting of a total of 446 galaxies, categorized by 34 with Lyα emission detected and 412 without Lyα emission. Finally, to further enhance the data set's reliability, we applied a stringent redshift cut, excluding sources lacking robust MOSDEF spectroscopic redshift determinations. This step led to the removal of five additional sources, yielding a final sample size of 451 galaxies, of which 29 were classified as Lyα-detected and 412 as Lyα nondetected.

3. Methodology

3.1. SED Fitting

To constrain the properties of stellar populations, we extended our analysis to encompass broadband photometry through the incorporation of the Bayesian SED fitting tool `Bagpipes`. This software leverages the 2016 spectral templates provided by G. Bruzual & S. Charlot (2003) and J. Chevallard & S. Charlot (2016), adopts the P. Kroupa (2001) initial mass function, and integrates nebular modeling via the 2017 version of CLOUDY (Ferland 2017). `Bagpipes` has the capacity to perform spectro-photometric fitting, allowing for simultaneous fitting of the spectra and photometry of a source, which we leverage in our study.

We opted for a flexible characterization of the star formation history (SFH) by employing a delayed-tau SFH model for fitting all galaxies, accommodating a wide range of SFH profiles, including rising and declining SFHs. The redshift was fixed at the spectroscopic redshift determined by MOSDEF. Since one of the outputs we get back from our nebular modeling algorithm is a measurement of the ionization parameter, we also fixed the ionization parameter in `Bagpipes` for sources that had good Hβ measurements (SNR > 5) to the emission-line-determined values in Section 3.2, and kept it a free parameter for those without good Hβ measurements, as seen in Table 1. Our photometric input for `Bagpipes` encompassed all available photometric measurements for each object from the 3D-HST catalog (R. E. Skelton et al. 2014; I. G. Momcheva et al. 2016). Moreover, to capitalize on `Bagpipes` spectro-photometric fitting capabilities, we incorporated all the sections of the MOSDEF spectra surrounding emission lines, within $\lambda_{\rm line} \pm 50$ Å, following the methodology outlined in A. C. Carnall et al. (2019). The inclusion of spectroscopic data introduces additional parameters in the fitting, essential for accounting for spectral noise, pixel correlations, and velocity dispersion. Detailed information on the parameters and their respective priors employed in our fitting process is presented in Table 1. With this approach, we are able to characterize the physical properties of the galaxies within our sample. For a more complete understanding of the implementation and modeling aspects, we direct the readers to the works of A. C. Carnall et al. (2018) and A. C. Carnall et al. (2019). This comprehensive approach utilizes both spectra and photometry to derive accurate estimates of the galaxy properties, and these estimates will be used to study their impact on Lyα observability.

Table 1
Bagpipes Parameters and Priors

Bagpipes Parameter	Range	Prior
Age	[0.01, 13] [Gyr]	Uniform
τ	[0.02, 14] [Gyr]	Uniform
Metallicity	[0, 2] [$Z/Z_\odot$]	Uniform
Mass-formed	[4, 13] [$\log_{10}(M/M_\odot)$]	Uniform
A_V	[0, 4] [Mag]	Uniform
log U	[−4, −2]	Uniform
Velocity Dispersion	[1, 1000] [km s^{-1}]	Uniform in $\log_{10}$
Calib 0	[0.5, 1.5]	$N(\mu = 1.0, \sigma = 0.25)$
Calib 1	[−0.5, 0.5]	$N(\mu = 0, \sigma = 0.25)$
Calib 2	[−0.5, 0.5]	$N(\mu = 0, \sigma = 0.25)$
Noise Scaling	[1, 10]	Uniform in $\log_{10}$

Notes. This table outlines the parameters and the corresponding priors used in the SED fitting with Bagpipes. Calib refers to the Polynomial calibration model used in `Bagpipes`to model spectroscopic systematics, using a second-order Chebyshev polynomial, with the number indicating the leading-order term. Calib 0 refers to the zero-order or P_0 term, Calib 1 is the first-order or P_1 term, and Calib 2 is the second-order or P_2 term.

`Bagpipes`, while a powerful tool for fitting galaxy properties, does not inherently consider systematic errors in the fitting process. To address this issue, we inflate the errors by 5% of the flux for non-IRAC bands and 20% of the flux for IRAC bands, as described in Equation (1), where $p_{\rm err}$ is the percent error for the associated band and $F_{\rm band}$ is the flux of the band, and σ is the original error from the photometry. This adjustment allows a better accounting for potential systematic uncertainties in our photometry. Following the fitting, `Bagpipes` provides a posterior distribution for each galaxy property, which we utilized to compare against various SED-derived properties, such as stellar mass and dust attenuation, as well as the output from our nebular line modeling algorithm. For reporting these values, we adopt the approach of using the median as our fiducial value, while the absolute difference between the median and the 16th and 84th percentiles served as the lower and upper errors for the respective galaxy properties:

$$\sigma = \sqrt{\sigma_{\rm original}^2 + (p_{\rm err}{}^*F_{\rm band})^2}. \quad (1)$$

To estimate the rest-frame Lyα equivalent width ($W_{\rm Ly\alpha}$) for galaxies within our sample, we implemented an approach based on the `Bagpipes` posterior model spectra. This process entailed computing the average continuum flux within the wavelength range of 1220–1250 Å in the rest frame. To account for the uncertainties inherent in the `Bagpipes` posterior models, we executed two distinct methods for deriving $W_{\rm Ly\alpha}$ while considering the associated posterior distributions.

Method 1 was applied to sources with Lyα detections in the HDR3 catalog. For these sources, we generated a posterior Lyα distribution by performing multiple random draws of the Lyα flux, each perturbed by the Lyα flux error assuming Gaussian uncertainties. The number of realizations was equal to the size of the continuum distribution, ensuring an appropriate match in distribution size. Method 2 was used on the non-Lyα-detected sources where our `emcee` Lyα line-fitting code had already produced a Lyα flux posterior distribution. These distributions were also made to match the size of the continuum distribution, ensuring consistent processing.

In both cases, we proceeded to compute a $W_{\rm Ly\alpha}$ posterior distribution by dividing the corresponding line flux distribution by the continuum distribution. To transform these values into rest-frame quantities, we divided the observed $W_{\rm Ly\alpha}$ distributions by $(1+z_{\rm sys})$, as shown in Equation (2). This method allowed us to derive a distribution of $W_{\rm Ly\alpha}$ values:

$$EW_{\rm Ly\alpha} = \frac{F\,({\rm Ly}\alpha)}{F_{\rm Continuum}(1+z_{\rm sys})}. \quad (2)$$

Many objects without a Lyα detection had rather high upper limits on $W_{\rm Ly\alpha}$ ($\geqslant$500 Å) caused by faint continuum fluxes. To ensure that our comparison between Lyα-detected and Lyα-nondetected samples are not skewed by these UV faint continuum sources, we further restrict the nondetected sources to those sources with an $W_{\rm Ly\alpha} < 20$ Å, a cut traditionally used to distinguish LAEs and non-LAEs (A. E. Shapley et al. 2003; C. Gronwall et al. 2007). This cut allows for a clear distinction for the nondetected, non-LAE sample, and by restricting our non-LAE sample only to those where we can conclusively show that any Lyα emission is weak, we create a more pure "control" sample. Applying this restriction on our nondetected sample provides our final sample size of 155 galaxies, with 126 sources in our Lyα-nondetected sample and 29 in our Lyα-detected sample.

3.2. Line Ratio Modeling

Here, we describe our process to model the rest-frame optical emission lines for galaxies in our sample, with the goal of unraveling the underlying factors that influence Lyα detectability. We compare our observed emission line fluxes with the line flux ratios predicted by the photoionization code MAPPINGS V (R. S. Sutherland & M. A. Dopita 2017). MAPPINGS V calculates line flux ratios relative to Hβ, with users having the flexibility to specify parameters including the ionizing radiation source, which can be either singular or composite, the radiation field geometry, providing options for spherical or plane–parallel configurations, and a comprehensive range of nebular characteristics, encompassing depletion timescales, dust grains, and elemental abundances.

These models utilize input ionizing spectra from Starburst99 (C. Leitherer et al. 1999), employing an E. E. Salpeter (1955) initial mass function and account for stellar mass loss. In tandem, MAPPINGS V leverages atomic data sourced from the CHIANTI 8 database (K. P. Dere et al. 1997; G. Del Zanna et al. 2015). This approach includes the application of photoionization, recombination, excitation, and dust depletion within a plane–parallel geometry to model H II regions and their ionizing spectra.

The MAPPINGS V models characterize their total metallicity Z in relation to solar values, but the relative abundances of individual elements are not simply scaled from solar abundances. At low metallicities, the MAPPINGS V models adopt α-enhanced abundances, as described in D. C. Nicholls et al. (2017), as the relative [O/Fe] abundance increases by 0.5 dex compared to solar when $Z/Z_\odot < 0.1$. The incorporation of α-enhancement at low metallicity in the MAPPINGS V models is supported by A. M. Amarsi et al. (2019) and aligns with observations of alpha enhancement in nebular emission. This phenomenon has been observed in both low-metallicity galaxies at $z \geqslant 2$ (e.g., C. C. Steidel et al. 2016; M. W. Topping et al. 2020; F. Cullen et al. 2021) and a detailed analysis of relative abundances in galaxies at $z > 5$ by K. Z. Arellano-Córdova et al. (2022).

While it is clear that the older Starburst 99 (SB99) cluster synthesis code (C. Leitherer et al. 1999) has been superseded in many ways by newer efforts such as the much more sophisticated BPASS code, we utilized the SB99 templates, as MAPPINGS V is currently implemented to only handle SB99 inputs. Active work is undergoing to incorporate BPASS templates (R. Sutherland 2024, private communication) but is currently not fully incorporated and tested. We acknowledge that SB99 may not be optimal for this analysis; however, it provides a relative comparison that should be taken with caution until new generation of large parameter space stellar atmosphere libraries are matched to evolutionary codes such as BPASS, MIST, SST, and other newer models.

Given the constraints posed by the limited number of available emission lines in our data set, we exercised the selection of a focused MAPPINGS V model grid. We use the pressure models of L. J. Kewley et al. (2019) for a grid of pressure $\log_{10}(P/k_{\rm B})$, ionization parameter $\log_{10}(Q)$,[12] and metallicity $Z/Z_\odot$. This grid incorporates variations in metallicity, spanning $Z/Z_\odot = [0.05, 0.2, 0.4, 1]$, and encompasses ionization parameter values within the range of $\log_{10}(Q) = [7, 8, 9]$. We chose a fixed ISM pressure at $\log_{10}(P/k_{\rm B}) = 6$, consistent with the prevalent conditions observed in star-forming galaxies, characterized by an electron density (n_e) of 100 cm^{-3} and an electron temperature (T_e) of 1×10^4 K, as corroborated by prior findings (B. Groves et al. 2008; R. Ahumada et al. 2020). Each of these grids provides a prediction of a large number of emission line fluxes (relative to Hβ). To match lines detectable in MOSDEF, we only use the lines provided in Table 2 in our final MAPPINGS V model grids.

Prior to using the `emcee` algorithm, we conducted a preparatory phase, involving the precomputation of theoretical flux ratios for every discernible emission line within the MOSDEF data set, detailed in Table 2. These computations encompassed every combination of metallicity and ionization

---

[12] We quantify ionization using $Q = \frac{L_{\rm HI}}{4\pi R^2 n_{\rm H}}$, noting that many papers also use $U = Q/c$ (or $\log U = \log[Q/({\rm cm\ s^{-1}})] - 10.48$) for ionization.

Table 2
MOSDEF Emission Line List

Line	Wavelength (Å)	# of Sources
[O II]λ3727	3726.032	98
[O II]λ3729	3728.815	106
[Ne III]λ3870	3868.764	37
[Ne III]λ3969	3967.471	10
Hδ	4101.742	31
Hγ	4340.741	18
[O III]λ4364	4363.209	2
Hβ	4861.333	102
[O III]λ4960	4958.911	106
[O III]λ5008	5006.843	139
[O I]λ6302	6300.304	18
[N II]λ6550	6548.052	30
Hα	6562.819	112
[N II]λ5685	6583.454	64
[S II]λ6718	6716.440	56
[S II]λ6733	6730.816	45

Note. Number of lines found from our sample of 155 galaxies after an SNR > 3 cut and galaxies with multiple emission lines appear in multiple rows.

parameter, resulting in the generation of an extensive grid of theoretical flux values. We match the observed lines to the model generated grids using the line species name paired with the wavelength. This method optimized the access to the relevant model grid within the `emcee` fitting routine.

We used the `emcee` algorithm to derive posterior constraints for the flux ratio model parameters. To enhance the precision of our analysis, we integrated the `RegularGridInterpolator` function from `scipy`, enabling us to perform linear interpolations of our model grids. This interpolation technique facilitated the exploration of a significantly more refined spectrum of ionization parameter and metallicity values.

One crucial parameter that MAPPINGS V does not include is dust attenuation, which we add into our model generation, as dust is certainly present in these galaxies and can heavily attenuate line emission. This effect introduces an additional free parameter to our model, the dust attenuation $E(B-V)$, where Equation (3) describes how a modeled flux ratio, $F_{\mathrm{model}}(\Theta)$, depends on the attenuation:

$$F_{\mathrm{model}}(\Theta) = F_{\mathrm{model}}(Q, Z)\,10^{-0.4(k(\lambda)-k(\mathrm{H}\beta))E(B-V)}. \tag{3}$$

This equation uses the extinction coefficients $k(\lambda)$ at a given wavelength λ and $k(\mathrm{H}\beta)$ assuming the D. Calzetti et al. (2000) dust attenuation law, using the wavelength 4861.363 Å for Hβ, as MAPPINGS V models predict line ratios relative to Hβ. $F_{\mathrm{model}}(Q, Z)$ represents the MAPPINGS V theoretical flux ratio prediction for a line at wavelength λ. The choice of the D. Calzetti et al. (2000) dust law was used because this is the same dust law used in our `Bagpipes` fitting and other dust laws such as the N. A. Reddy et al. (2020) dust law produce a negligible change in the modeled flux and do not alter the end results.

3.2.1. Priors

Our nebular line modeling algorithm imposes a set of priors to constrain certain galaxy properties, such as dust. Over 70% of the sources in our sample have Hα and Hβ flux measurements, which allows us to directly compute a measurement of the dust, via the Balmer decrement. When both of these lines are detected at an SNR > 5, we measure the Balmer decrement, use a Gaussian prior for the $E(B-V)$ dust measurement that is centered on the Balmer decrement value, and use the uncertainty in the Balmer decrement calculation as the σ in the Gaussian prior. However, there are sources where Hα or Hβ are not present in the spectrum, due to falling between the spectroscopic bands or because the lines are not at a high enough significance to provide robust flux measurements. For these sources, we impose a log uniform prior, which gives higher probability for low $E(B-V)$ values while allowing `emcee` to explore higher $E(B-V)$ values at a lower probability. We used the `scipy` *stats* package, used the log uniform class to compute the probability from this prior, and used the following input parameters that control the shape and location of the distribution: $a = 0.2$, $b = \mathrm{e}$ (the irrational number), loc $= -0.1$, and scale $= 0.45$. Where a and b control the properties of the probability distribution as shown in Equation (4), loc controls the horizontal shift of the distribution and scales, stretches, or compresses the input values when computing the probability distribution function via Equation (5):

$$P(x|a, b) = \frac{1}{x\ln(b/a)} \tag{4}$$

$$P(y|a, b) = \frac{1}{y\ln(b/a)},\ \text{where } y = \frac{x - \mathrm{loc}}{\mathrm{scale}}. \tag{5}$$

For the other parameters such as $\log_{10}(Q)$ and metallicity (Z), we utilized a uniform prior on these parameters within the bounds of the grid shown in Figure 1. These bounds were $\log_{10}(Q) = [7, 9]$ and metallicity $(Z) = [0, 1]$

For our likelihood function, we assume that the measurement and subsequent error follow a normal distribution. The likelihood function, after performing the maximum-likelihood estimates, is represented by Equation (6):

$$\ln p(F_n|\ \sigma_n, \Theta)) = -\frac{1}{2}\sum_n\left[\frac{(F_n - F_{\mathrm{model}}(\Theta))^2}{\sigma_n^2} + \ln(2\pi\sigma_n^2)\right], \tag{6}$$

which is similar to minimizing the chi-squared across all the lines in the spectrum. Here, F_n represents the observed flux ratio for a specific line relative to Hβ, while Θ denotes the model parameter values ($\log_{10}(Q)$, $Z/Z_{\odot}$, and $E(B-V)$). $F_{\mathrm{model}}(\Theta)$ corresponds to the theoretical model flux ratio, derived from the MAPPINGS V model grids, based on the provided values of $\log_{10}(Q)$, $Z/Z_{\odot}$, and $E(B-V)$, as defined in Equation (3). Additionally, σ represents the error associated with the observed line ratio relative to Hβ.

Our methodology can perform fitting for a wide range of input lines, incorporating all possible line ratios into the fitting routine. However, it is crucial to exercise caution, as unreliable detections may introduce bias into the fit. As a precaution, we restrict our analysis to lines with robust detections, characterized by an SNR > 5.

3.2.2. Verification Checks

We describe the results of a diagnostic test, to explore the performance of our algorithm when fitting all available lines, versus a smaller set. The results of this validation are presented in Figure 1, where we specifically focus on the [O III]λ5007/Hβ versus Ne IIIλ3870/[O II]λ3727, commonly referred to as

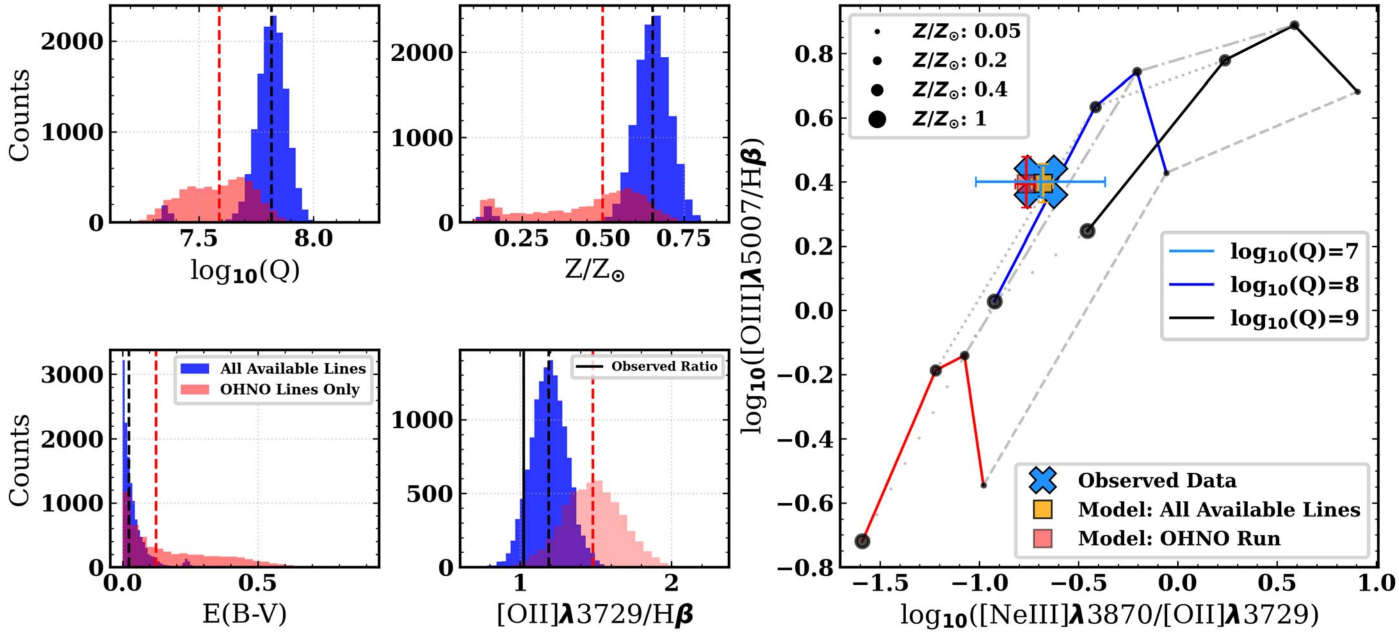

Figure 1. Left: Posterior distributions of the parameters in our nebular modeling code and line fluxes using all available lines in blue and only [O III]λ5007, Hβ, Ne IIIλ3870, and [O II]3729 in red for single sources. We achieve greater constraints on the physical properties when all available lines are used over a subset of lines. Right: We present the model grid used in our nebular modeling algorithm, comparing predictions for line flux ratios based on the best-fit results using only the "OHNO" lines as input vs. using all available lines. We can see that both model predictions overlap the observed data within the error bars; however, due to the tighter constraints on nebular line properties, we use the run using all available lines.

the"OHNO" diagram (J. R. Trump et al. 2023; B. E. Backhaus et al. 2024). We performed two distinct runs with our algorithm: one utilizing solely the lines within the "OHNO" diagram and the other considering all available lines in the spectrum so long as either the [O III]λ5007 or Hα had an SNR greater than 5.

After conducting this run, we used the posterior parameters values returned from our nebular line modeling algorithm and generated model flux predictions for [O II]λ3729. We show in the left panel of Figure 1 the posterior distributions between using a subset of lines against using all available lines. We highlight that the posterior distributions for the parameters are quite different, with the OHNO-only lines being broader than using all available lines, and this underscores the importance of using all available lines in the spectra to constrain galaxy properties using our algorithm. We show in the bottom right panel of Figure 1 the model flux predictions of the [O II]λ3729 line and compare each run with the observed ratio from the spectrum. We show that the median of the distribution using all available lines is much closer to the actual data value than that obtained using only a subset of lines. While our model tends to overpredict [O II]λ3729, there is part of the distribution at the observed data value. This validation process showcases the algorithm's capacity to reproduce observed line ratios and highlights the critical role that the input emission lines have in our analysis. For our analysis, we use the full suite of lines available to us when running our algorithm and quote the best-fit parameter value. The final number of sources that we were able to run this nebular analysis on was 26 out of 29 Lyα-detected sources and 109 out of 126 Lyα-nondetected sources, with those omitted caused by a combination of Hβ falling between the band gaps and nebular lines having a low SNR ($\mathrm{SNR} < 5$).

4. Results

We present the results of our analysis split into two parts: the first portion covers differences in galaxy properties between the Lyα-detected and Lyα-nondetected sources. The second portion focuses only on the Lyα-detected sample for Lyα specific results, such as Lyα velocity offsets and $f_{\mathrm{esc}}^{\mathrm{Ly}\alpha}$.

In our procedure, we have acquired constraints on properties through spectro-photometric SED fitting, and some through our nebular modeling of the emission lines. The properties and units obtained from SED fitting are stellar mass in units of $\log_{10}(M/M_\odot)$, dust attenuation A_V in units of mag, SFRs in units of $M_* \mathrm{yr}^{-1}$, metallicity ($Z/Z_\odot$), and specific SFR (sSFR) in units of yr^{-1}. From our nebular line modeling code, we obtain the ionization parameter represented as $\log_{10}(Q)$, which relates to the dimensionless ionization parameter U via $U = Q/c$, metallicity ($Z/Z_\odot$), and dust via $E(B-V)$. We emphasize that, while both SED fitting and our nebular fitting algorithms constrain metallicity, the value of metallicity, unless otherwise stated in the text, will be derived from the nebular line modeling algorithm, as this approach provides a more robust measurement.

4.1. Differences between Lyα Detected and Nondetected

In this study, we investigate the physical distinctions between the samples of galaxies with and without detectable Lyα emission. To quantify these differences, we take the posterior distributions from the `Bagpipes` fits and the emcee chains from the nebular line algorithm for each galaxy within our sample and draw 5000 random samples from the posterior distribution. Subsequently, we constructed two matrices, each with dimensions $N \times M$, where N represents the number of galaxies in the Lyα-detected and nondetected samples, respectively (comprising 29 and 126 sources), and M corresponds to the number of posterior draws (5000). For each of the posterior draws, we conducted Kolmogorov–Smirnov (KS) tests between the two populations, assessing whether their physical properties are statistically different. This process generated 5000 KS statistics along with their corresponding p-values. Table 3 provides the median values and associated errors for both quantities. For the two populations

Table 3
KS Statistics and P-values

Parameter	KS Statistic	P-value
$W_{\mathrm{Ly}\alpha}$	$0.74^{+0.03}_{-0.04}$	$2.4^{+77.7}_{-2.3} \times 10^{-13}$
Mass	$0.39^{+0.025}_{-0.02}$	$0.006^{+0.006}_{-0.003}$
A_v	$0.30^{+0.03}_{-0.02}$	$0.06^{+0.04}_{-0.03}$
sSFR	$0.26^{+0.03}_{-0.03}$	$0.16^{+0.11}_{-0.08}$
Q	$0.25^{+0.06}_{-0.05}$	$0.21^{+0.28}_{-0.14}$
Z	$0.26^{+0.06}_{-0.05}$	$0.16^{+0.23}_{-0.11}$

Notes. A table of the KS statistics and the corresponding P-values for the `Bagpipes` and MAPPINGS V `emcee` parameter values. A p-value of $\leqslant 0.05$ indicates that the two populations are different at the $\geqslant 2\sigma$ level. The results of the KS test show that stellar mass, Dust A_V, and SFR are different between the Lyα-detected and nondetected populations.

to be considered statistically different, we require that the p-value fall below the 0.05 threshold, signifying a less than 5% probability that the two samples share a common parent distribution.

To illustrate the differences between the two samples, we computed the cumulative distribution functions (CDFs) based on the `Bagpipes` and nebular line modeling posterior distributions of various derived galaxy properties using the $N \times M$ matrix, outlined in the previous paragraph, for each galaxy property. For every posterior draw, the CDFs were computed by binning the distributions and then performing a cumulative summation of the distributions, normalized by the total sum across all the bins, yielding a total of 5000 CDFs for both the Lyα-detected and nondetected samples. The results of the CDFs for the Lyα-detected and nondetected sample are presented in Figure 2, where the the shaded region illustrates the 1σ ranges of these CDFs for the two samples.

In the first panel of the top row of Figure 2, a property that presents slight visual differentiation between the two samples is the ionization parameter $\log_{10}(Q)$. The Lyα-detected sample reaches a threshold of 50% at a slightly higher ionization parameter compared to the nondetected sample; however, the KS statistic and corresponding p-value suggest that both distributions originate from a common parent distribution, with a KS statistic of 0.25 and a p-value of 0.21. Nonetheless, it is still noteworthy that the 1σ spread of the CDFs exhibits limited overlap between $\log_{10}(Q) = 7.4$–8.6, indicating a difference between the two samples. This subtle distinction may provide insight into the presence or absence of Lyα emission between these samples.

The next parameter that exhibits some visual differences between the two samples is the metallicity determined by our nebular line modeling algorithm. The second panel of the top row of Figure 2 shows that the Lyα-detected sample tends to display, on average, lower metallicity compared to the Lyα-nondetected sources. However, upon subjecting these distributions to the KS test, the results indicate a 16% likelihood of both distributions originating from the same parent distribution under random sampling, which exceeds our significance threshold of 5% to conclude they are different distributions. While we cannot reject the null hypothesis that these two distributions are drawn from the same distribution, the 1σ shaded region in top middle panel of Figure 2 does start to diverge at around $0.3\,Z/Z_{\odot}$ between the two samples, pointing to a difference in this metallicity regime between the Lyα-detected and nondetected sample.

The leftmost panel on the bottom row shows a strong contrast between the Lyα-detected and nondetected as the two CDFs have little to no overlap throughout the explored $W_{\mathrm{Ly}\alpha}$ range. This discrepancy is reaffirmed by the KS statistic, calculating a p-value of 2.4×10^{-13}, far below our minimum threshold of 0.05. This result is unsurprising, as we have constructed this $W_{\mathrm{Ly}\alpha}$ cut between the Lyα-detected and nondetected sample.

Another property exhibiting a substantial contrast between the two populations is stellar mass, as depicted in the second panel on the bottom row of Figure 2. The Lyα-detected galaxies consistently tend toward lower mass values compared to their nonemitting counterparts. This trend is evident in the CDFs, where the Lyα-detected sample's posterior distributions reach the 50th percentile at a much lower stellar mass than the nondetected sample, resulting in a distinct separation between the two. Statistically, this distinction is highlighted by the KS statistic, which returns a value of 0.39 along with a p-value of 0.006, well below our 0.05 threshold for a 2σ significance to reject the null hypothesis. These results signify that the two samples originate from different distributions, highlighting the importance that stellar mass has for Lyα observability. This study is subject to the constraints of a luminosity-selected and consequently mass-selected sample, owing to the MOSDEF H-band selection criteria. While this feature imposes restrictions on the range of mass values examined, it affords the advantage of comparing the physical properties of galaxies within a similar mass range, thereby facilitating the identification of key factors influencing Lyα emission.

Another physical property that, by eye, distinguishes Lyα-detected galaxies from their nonemitting counterparts is the dust attenuation, quantified by the A_V and derived by `Bagpipes`. This contrast is vividly portrayed in the bottom row of the third panel of Figure 2. The CDFs of the Lyα-detected galaxies demonstrate a steeper slope, indicating that the majority of the posterior distribution for this population is concentrated at lower A_V values: the 50th percentile is at much lower dust attenuation than the nonemitted sample. Furthermore, the CDFs of the Lyα-detected galaxies exhibit little overlap with the CDFs of the nonemitting galaxies within the A_V range of 0 to 0.75. This visual disparity, however, is just shy of being statistically significant in terms of the KS statistics, which yield a value of 0.30 with a p-value of 0.06. While it is not at a robust 2σ significance, it is well above 1σ and does point to dust playing a major role in reducing the observability of Lyα in the nondetected sample. A curious aspect is that there does appear to be a difference between SED-derived dust and nebular dust measurement. This difference is most likely attributable to the difference in dust attenuation experienced between the stellar and nebular components. The literature has shown that nebular lines have measured higher dust attenuation than the SED (see D. Calzetti et al. 2000; V. Wild et al. 2011; L. Rodríguez-Muñoz et al. 2022) and have demonstrated that nebular-derived dust measurements calculate more dust, typically giving ratios of dust excess $E(B-V)_{\mathrm{stellar}}/E(B-V)_{\mathrm{nebular}} \sim$ 0.44–0.64.

The bottom right panel of Figure 2 shows the CDF distributions for the `Bagpipes`-derived sSFR. There are some differences in the CDFs between the Lyα-detected and nondetected sample at high sSFR. This difference indicates that the Lyα-detected sources preferentially have, on average, a higher sSFR than their nondetected counterparts. While the CDFs suggest that there is some difference between the two

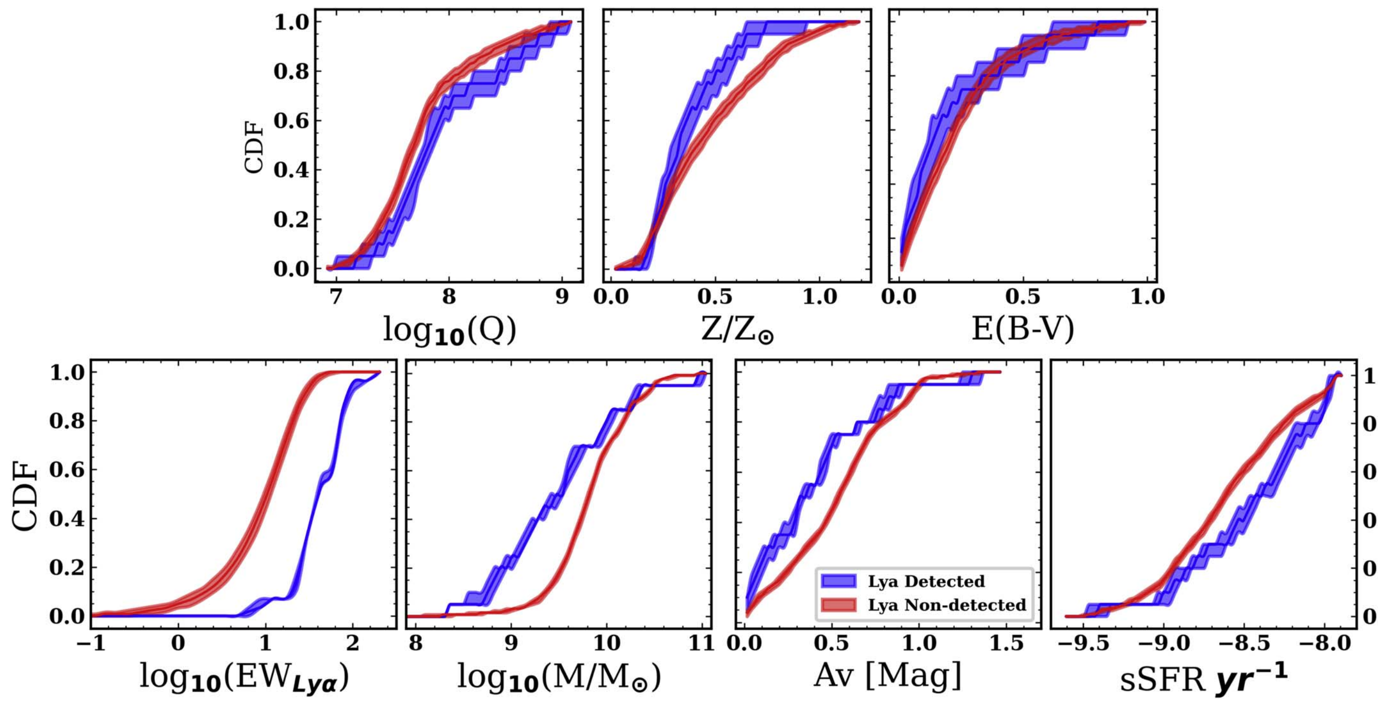

Figure 2. The CDFs for various galaxy properties from nebular line modeling algorithm are given in the top row and `Bagpipes` in the bottom row. The blue and red shaded curves correspond to the 1σ spread in the CDFs for the Lyα-detected and nondetected samples, respectively. The CDFs show clear evidence of physical differences between the two samples. The top row panels suggests differences between the ionization parameter [$\log_{10}(Q)$] and metallicity. In the bottom row, the differences are even more stark; there are physical differences between the two samples in terms of the Lyα equivalent width, stellar mass, dust attenuation, and specific star formation rate. The top row shows some tentative differences; the KS test returned p-values above 0.05, [Q: 0.25, p-val: 0.21, Z: 0.26, p-val: 0.16, $E(B-V)$: 0.27, p-val: 0.34], indicating there is a high probability the two distributions are drawn from the same distribution. The `Bagpipes`-derived properties had the following KS statistics: $W_{\mathrm{Ly}\alpha}$: 0.74, p-val: 2.4×10^{-13}, Stellar mass: 0.39, p-val: 0.006, Av: 0.30, p-val: 0.06, sSFR: 0.26, p-val: 0.16. Indicating that a main contributor to the observability of Lyα is the stellar mass and lack of dust.

samples, when the KS test is applied on this parameter, there is evidence that these two distributions can be drawn from the same distribution. The KS test computed a statistic of 0.26 with a p-value of 0.16, well above the 0.05 p-value threshold we required for them to be drawn from different distributions, and proves statistically that sSFR can be drawn from the same distribution between the two.

In our analysis, a clear distinction emerges between the Lyα-detected and nondetected galaxy samples, with some exhibiting striking differences ($\geqslant 2\sigma$), while others show more subtle disparities ($\leqslant 1\sigma$). The most pronounced distinctions are observed in the equivalent width ($W_{\mathrm{Ly}\alpha}$) and stellar mass. These properties exhibit evident separations, signifying significant differences between the two populations. Dust is just shy of the 2σ significance but is considered to be an important parameter that regulates Lyα emission. We also explored properties such as ionization parameter ($\log_{10}(Q)$) and metallicity, where subtle variations are perceptible, although they do not reach statistical significance in the KS tests. The complete results of our KS-statistical analysis are presented in Table 3, accompanying the visual representations in Figure 2.

4.2. Lyα-detected Sources

By focusing on a specific subset of galaxies with detectable Lyα emission, our study presents a unique opportunity to delve into the intricate interplay between the ISM conditions and Lyα escape. Leveraging the data set provided by MOSDEF and HETDEX, we not only discern the Lyα velocity offset from the systemic velocity but also determine the Lyα escape fraction by examining Balmer emission lines. These measurements will aid to enhance our insights into the astrophysical processes governing Lyα emission.

4.2.1. Lyα Velocity Offset

The precision of the spectroscopic redshift data obtained from MOSDEF enables an assessment of the Lyα velocity offset. This offset is determined by quantifying the difference between the systemic redshift, as measured by rest-frame optical nebular lines, such as Hβ and/or [O III]λ5007, and the spectroscopically derived Lyα redshift via Equation (7), which accounts for cosmological and relativistic effects. The presence of such discrepancies can be attributed to intricate dynamics within the galaxy, involving processes such as outflows or inflows within the ISM:

$$\Delta v_{\mathrm{Ly}\alpha} = \frac{(1 + z_{\mathrm{Ly}\alpha})^2 - (1 + z_{\mathrm{sys}})^2}{(1 + z_{\mathrm{Ly}\alpha})^2 + (1 + z_{\mathrm{sys}})^2} \cdot c. \qquad (7)$$

In Equation (7), $z_{\mathrm{Ly}\alpha}$ represents the redshift determined from the Lyα emission line, obtained through the HETDEX observations, z_{sys} corresponds to the spectroscopic redshift measured by MOSDEF, and c denotes the speed of light. We compute the Lyα velocity offset for every Lyα-detected galaxy in our sample and present the findings in Figure 3. We measure a median Lyα velocity offset of 177.70 km s^{-1} with typical uncertainties around 47.7 km s^{-1}, which hold consistently with what D. Davis et al. (2023b) found in their stack of 50,000 HETDEX LAEs. Some of the sources show signs of being

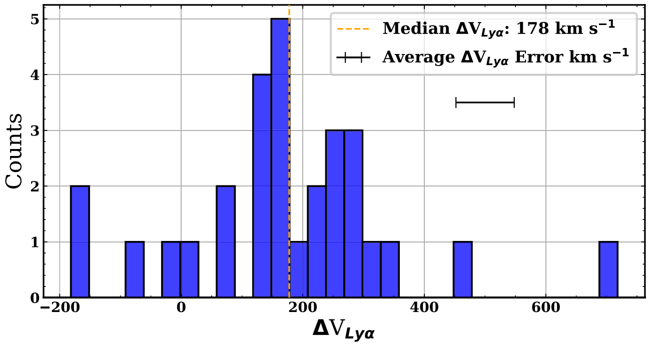

Figure 3. Histogram showing the velocity offset computed using Equation (7). Most of the Lyα-detected sources are redshifted from systemic with a median velocity offset of $+178$ km s^{-1}, and we show the typical uncertainty in the velocity offset, which is 47.7 km s^{-1}.

blueshifted, which is indicative of Lyα backscattering due to inflows.

4.2.2. Lyα Escape Fraction

We further expand our Lyα analysis by using our two samples to estimate their Lyα escape fraction ($f_{\rm esc}^{\rm Ly\alpha}$) (summarized in Figure 4). For the nondetected sample, the upper limit on the Lyα flux was computed during our initial Lyα line search. Our approach, based on the methodology of D. Sobral & J. Matthee (2019), calculates $f_{\rm esc}^{\rm Ly\alpha}$ for sources with detectable Hα measurements, as detailed in Equation (8):

$$f_{\rm esc}^{\rm Ly\alpha} = \frac{L_{\rm Ly\alpha}}{8.7 L_{\rm H\alpha} \times 10^{0.4\times A_{\rm H\alpha}}}. \tag{8}$$

To determine $f_{\rm esc}^{\rm Ly\alpha}$, we convert the observed Hα fluxes to Hα luminosity using the luminosity distance at the redshift provided by MOSDEF. Additionally, we employ A(Hα) for the dust attenuation correction, where A(Hα) is computed as the product of $k(\lambda_{\rm H\alpha})$ and $E(B-V)$. Here, $k(\lambda_{\rm H\alpha})$ represents the dust attenuation at the Hα wavelength, assuming a D. Calzetti et al. (2000) extinction law, and $E(B-V)$ is the maximum-likelihood value from our nebular fitting algorithm. The factor of 8.7 reflects the expected intrinsic ratio of $F({\rm Ly}\alpha)/F({\rm H}\alpha)$ based on Case B recombination (R. M. Pengelly 1964; P. J. Storey & D. G. Hummer 1995). For cases where Hα measurements are undetectable, due to Hα falling in detector gaps between the different bands or at a low significance, we compute $f_{\rm esc}^{\rm Ly\alpha}$ using Hβ, as outlined in L. H. Weiss et al. (2021), with an assumed intrinsic Lyα/Hβ ratio of 23, and we also correct for dust using the $E(B-V)$ value acquired from our MAPPINGS V `emcee` fitting algorithm.

We test the assumption that these galaxies are in the low electron density ($n_{\rm e}$) limit where case B is assumed. We use the density-sensitive diagnostic [O II]$\lambda3729/\lambda3726$ line ratio, and only include galaxies with [O II]$\lambda\lambda3726$, 3729 line fluxes that have SNR $\geqslant 3$. To derive $n_{\rm e}$, we use the nebular analysis package `PyNeb` (V. Luridiana et al. 2015, version 1.1.18) and make use of atomic data for O$^+$; the data are from C. Froese Fischer & G. Tachiev (2004) for transition probabilities and R. Kisielius et al. (2009) for collision strengths. Due to the low SNR of the temperature-sensitive auroral line [O III]$\lambda4363$, we are not able to get accurate electron temperatures ($T_{\rm e}$) and densities together, so we use the *getTemDen* task to compute $n_{\rm e}$ assuming that $T_{\rm e} = 10{,}000$ K. R. L. Sanders et al. (2016) make the same assumption for a sample of MOSDEF galaxies. We find that most of the galaxies we compute $f_{\rm esc}^{\rm Ly\alpha}$ for do fall in the low-density limit.

To investigate the factors influencing the escape of Lyα emission, we conducted an analysis of $f_{\rm esc}^{\rm Ly\alpha}$ in conjunction with several key galaxy properties, including $W_{\rm Ly\alpha}$ stellar mass, SFR, dust attenuation (A_V) derived from `Bagpipes`, and the ionization parameter derived from our nebular line modeling routine (see Figure 4). Our examination involved assessing the strength of these relationships using correlation coefficients.

Given the constraints imposed by our relatively modest sample size (155), we adopted a permutation test approach, as recommended by the documentation of the “spearmanr” function in `scipy`, to compute the correlation coefficients. We categorized the correlation strength into three bins: weak ($|\rho| < 0.3$), moderate ($0.3 \leqslant |\rho| \leqslant 0.6$), and strong ($|\rho| > 0.6$), with robust significance for these correlations established when the associated p-value fell below 0.05.

Our analysis uncovered several notable properties exhibiting moderate correlations with $f_{\rm esc}^{\rm Ly\alpha}$ as summarized in Table 4. We measure a moderate, positive correlation between $f_{\rm esc}^{\rm Ly\alpha}$ and $W_{\rm Ly\alpha}$, with a Spearman-r correlation coefficient of 0.36 and a p-value of 0.00007, indicating a high significance for the association between $f_{\rm esc}^{\rm Ly\alpha}$ and $W_{\rm Ly\alpha}$. Moreover, a positive correlation is also observed between $f_{\rm esc}^{\rm Ly\alpha}$ and the ionization parameter, with a Spearman's correlation coefficient of 0.33 and a p-value of 0.0002. There are moderate anticorrelations between $f_{\rm esc}^{\rm Ly\alpha}$ and other galaxy properties; in particular, there is a moderate anticorrelation between $f_{\rm esc}^{\rm Ly\alpha}$ and stellar mass, with a Spearman's correlation coefficient of -0.34 and a p-value of 0.0001. Similarly, $f_{\rm esc}^{\rm Ly\alpha}$ exhibits negative correlations with SFR (Spearman-r: -0.38, p-value: 0.00002) and the `Bagpipes`-derived dust measurement A_V (Spearman-r: -0.41, p-value: 0.000003), as illustrated in Figure 4. There is no evidence of a correlation existing between $f_{\rm esc}^{\rm Ly\alpha}$ and the Lyα velocity offset, with a Spearman correlation of -0.06 and a p-value of 0.79.

5. Discussion

5.1. The Effect of Mass

Numerous spectroscopic investigations of LAEs (e.g., S. L. Finkelstein et al. 2009; R. F. Trainor et al. 2016; A. L. Strom et al. 2017; M. Ouchi et al. 2020; R. Pucha et al. 2022) consistently reveal a prominent trend: LAEs typically exhibit lower masses compared to other continuum-selected star-forming galaxies. This pattern also emerges from our analysis, where Lyα-detected sources exhibit, on average, lower masses than their nondetected counterparts. The lower mass of these galaxies offers distinct advantages in the context of Lyα observations. The first advantage is that lower-mass galaxies will have a lower gravitational potential, making it easier for high-energy events such as supernovae, AGN feedback, and radiation pressure to clear out the surrounding material and facilitating the creation of open channels that promotes Lyα escape as supported by previous studies (K. Nakajima & M. Ouchi 2014; H. Yajima et al. 2014; M. Dijkstra et al. 2016; A. Smith et al. 2022).

An additional way in which low-mass galaxies promote Lyα escape is via the well-established mass–dust relationship (N. Bourne et al. 2012; P. Santini et al. 2014; K. E. Whitaker et al. 2017). Since lower-mass galaxies tend to harbor less dust, the likelihood of Lyα absorption is reduced and further

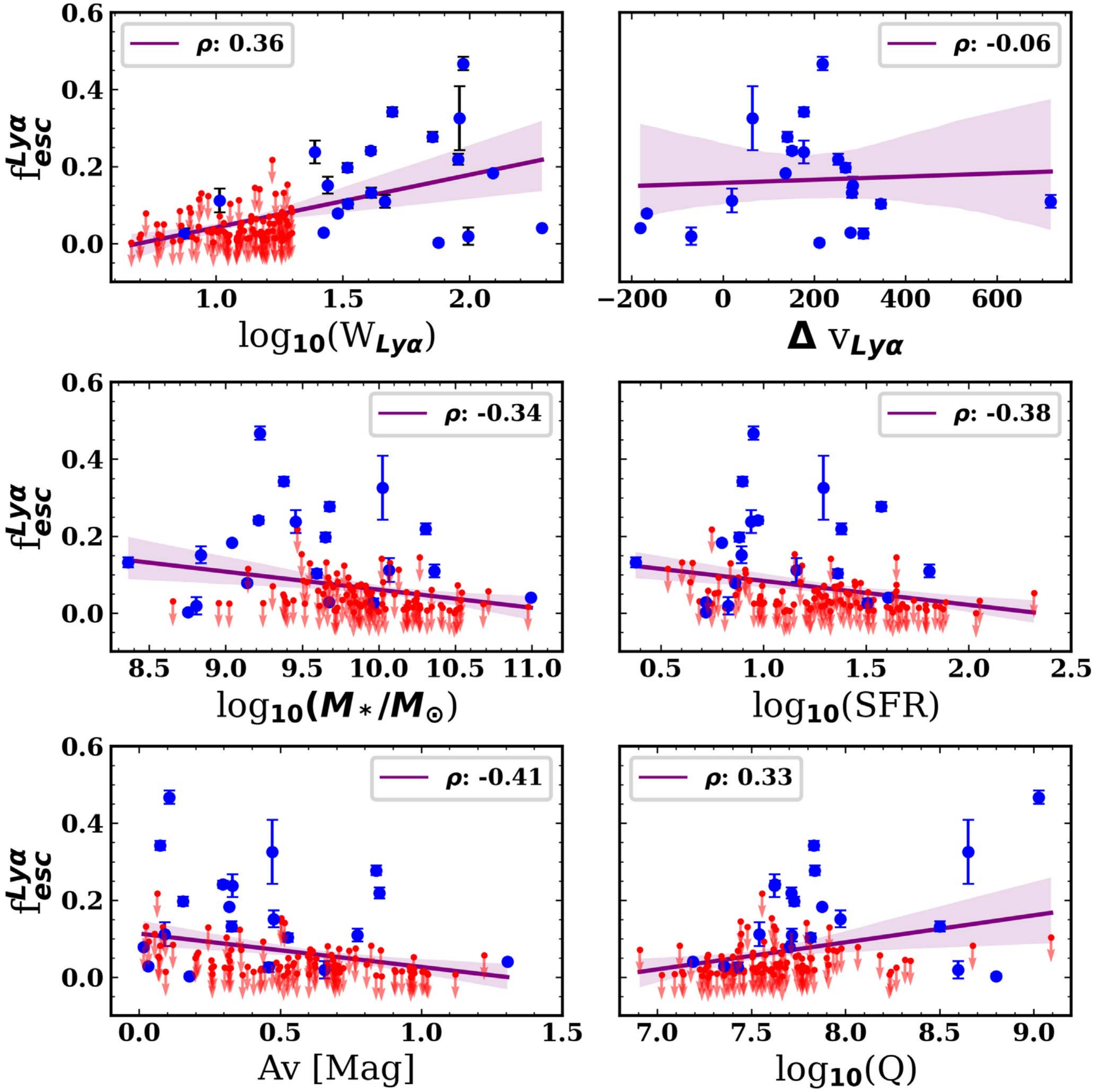

Figure 4. This set of panels showcases the correlations between $f_{\rm esc}^{\rm Ly\alpha}$ and various galaxy properties, where the Lyα-detected sample is shown in blue and the nondetected galaxies are given by red downward arrows indicating their upper limit on $f_{\rm esc}^{\rm Ly\alpha}$. The purple shaded regions are the 1σ spread on the correlation using the Lyα-detected and nondetected samples, and the solid purple line is the best-fit line. The quantity $f_{\rm esc}^{\rm Ly\alpha}$ is positively correlated with the Lyα equivalent width and ionization parameter [$\log_{10}(Q)$] at high significance (p-values of 0.00007 and 0.0002, respectively). There are convincing anticorrelations between $f_{\rm esc}^{\rm Ly\alpha}$ and stellar mass, SFR, and `Bagpipes`-derived dust attenuation measuring −0.34 (p-value: 0.00015), −0.38 (p-value: 0.00002), and −0.41 (p-value: 0.000003). There are no correlations between $f_{\rm esc}^{\rm Ly\alpha}$ and the velocity offset of Lyα measuring −0.06 (p-value: 0.78).

enhances its escape probability. This is most evidently seen in multiple prior studies reporting anticorrelations between Lyα equivalent width and dust properties (H. Atek et al. 2008; K. A. Kornei et al. 2010; R. F. Trainor et al. 2016; X. Du et al. 2021; O. A. Chavez Ortiz et al. 2023). For example, X. Du et al. (2021), analyzing galaxies from the MOSDEF sample and following up with UV LRIS spectroscopy, found a general anticorrelation in their sample between $W_{\rm Ly\alpha}$ and $E(B-V)$. Their sample also included sources with Lyα in absorption and emission, whereas our sample is only sensitive to Lyα in emission. The same dust trends seen in these other studies are visible in our sample, where the Lyα-detected galaxies are on average less dusty than the nondetected sample. Dust has also been shown in theoretical models of Lyα radiative transfer to suppress or even completely remove Lyα emission along the line of sight (A. Verhamme et al. 2006; H. Yajima et al. 2012). Our findings corroborate this interpretation, especially when examining the results in Figure 4, which show a strong anticorrelation between $f_{\rm esc}^{\rm Ly\alpha}$ and the `Bagpipes`-derived dust measurements.

Table 4
$f_{\rm esc}^{\rm Ly\alpha}$ Correlation Results

Parameter	Spearman-r	P-value
$W_{\rm Ly\alpha}$	+0.36	0.00007
$\Delta v_{\rm Ly\alpha}$	−0.06	0.79
$\log_{10}(M/M_\odot)$	−0.34	0.00015
SFR	−0.38	0.00002
A_V	−0.41	0.000003
$\log_{10}$(Q)	+0.33	0.0002

Notes. A table of Spearman-r correlation coefficients and their corresponding p-values after performing the `scipy` permutation test on $f_{\rm esc}^{\rm Ly\alpha}$ and various galaxy properties. A moderate anticorrelation exists between stellar mass, dust attenuation A_V, and SFR, and a moderate correlation between $W_{\rm Ly\alpha}$ and $\log_{10}(Q)$. There is no correlation between $f_{\rm esc}^{\rm Ly\alpha}$ and Lyα velocity offset.

Low-mass galaxies also offer a compelling advantage for enhancing Lyα emission, primarily due to their lower metallicity, a consequence of the well-established mass–metallicity relationship (D. K. Erb et al. 2006; L. J. Kewley & S. L. Ellison 2008) and further found in the MOSDEF sample in R. L. Sanders et al. (2020). The reduced metallicity in these galaxies results in a harder ionizing spectrum emitted by their stars, characterized by a greater abundance of ionizing photons compared to higher-metallicity environments, where metals can absorb and diminish the ionizing radiation (N. Kumari et al. 2021). This enhanced ionizing radiation, in turn, maintains a larger fraction of the interstellar hydrogen in an ionized or excited state, significantly improving the escape probability of Lyα photons through ease of transmission and through an increase in recombination (M. Dijkstra 2014). Seeing this effect of mass in our sample is intriguing since the parent sample that the Lyα-detected and Lyα nondetected samples come from is a magnitude-limited and by proxy a mass-limited sample, making this mass dependence a true feature rather than a selection effect. In summary, the unique environment of low-mass galaxies provides the ideal conditions to facilitate the escape of Lyα radiation.

5.2. The Effect of Metallicity and Ionization Parameter

In our study, an intriguing discovery emerges as we explore the Lyα-detected sample. The Bayesian nebular line modeling algorithm appears to favors models characterized by low metallicity and high ionization parameters for the Lyα-detected sample, as illustrated in Figure 2. This preference, albeit at a somewhat tentative 1σ confidence, hints at the pivotal role these two parameters play in enhancing the detectability of Lyα in our sample. The link between lower metallicity and higher ionization parameter is direct, as outlined in the previous paragraph. The combined effect of these factors significantly enhances the amount of Lyα produced and increases the prevalence of Lyα via recombination in the ISM, consequently elevating the likelihood of Lyα escaping into the circumgalactic medium (CGM).

The influence of a high ionization parameter and low metallicity on enhancing Lyα detectability has been a recurring theme in prior research, aligning with the notable high $W_{\rm Ly\alpha}$ values observed. Studies such as those conducted by D. K. Erb et al. (2016) and R. F. Trainor et al. (2016) have independently provided converging evidence that galaxies characterized by a high ionization parameter and low metallicity exhibit enhanced Lyα emissions, as evident from their measured $W_{\rm Ly\alpha}$. These studies employed diverse LAE selection criteria—R. F. Trainor et al. (2016) used narrowband (NB) techniques, selecting bright continuum sources, while D. K. Erb et al. (2016) relied on photometric UV-color cuts and BPT diagnostics to find LAEs. Further supporting this pattern, K. Nakajima et al. (2013) observed analogous results in their study of NB-selected LAEs, where they reported that their spectroscopic data pointed to these sources exhibiting low metallicity and a high ionization parameter. Despite the differences in selection methodologies, a consistent narrative emerges in that LAEs typically exhibit a higher ionization parameter, underscoring the robustness of these trends within the LAE population.

5.3. Discussion on Lyα-derived Properties

The study of Lyα escape and its ties to galaxy properties is necessary to understand the mechanism(s) that facilities its observability. In our Lyα-detected sample there are clear trends with $f_{\rm esc}^{\rm Ly\alpha}$ and various galaxy properties, the most notable of which is the positive correlation between the Lyα equivalent width and the ionization parameter. There is also clear evidence of a moderate anticorrelation between stellar mass, SFR and `Bagpipes`-derived dust to $f_{\rm esc}^{\rm Ly\alpha}$. These correlations and anticorrelations hint that these galaxy properties are crucial in aiding the observability of Lyα.

Compelling evidence from prior Lyα studies bolsters our findings and provide insights into our measurements. For instance, work on $z \sim 2$ galaxies, such as H. Atek et al. (2009), M. Hayes et al. (2011), J. Matthee et al. (2016), N. A. Reddy et al. (2016), and L. H. Weiss et al. (2021), find that galaxies tend to have a negative correlation between $f_{\rm esc}^{\rm Ly\alpha}$ and dust, hinting at a fundamental link between Lyα escape and the lack of dust. These findings are consistent with models where a lack of internal dust reduces the impact of Lyα absorption within the galaxy and makes the likelihood of Lyα escaping much higher. Interestingly, L. H. Weiss et al. (2021) and J. Matthee et al. (2016) offer different results when it comes to $f_{\rm esc}^{\rm Ly\alpha}$ and its link with stellar mass. L. H. Weiss et al. (2021) shows clear anticorrelation with stellar mass, similar to work from A. J. Pahl et al. (2023), whereas J. Matthee et al. (2016) suggest only a slight decrease with increasing mass. This disparity of results may be attributable to the differing selection techniques: J. Matthee et al. (2016) found sources via NB imaging of Hα emission, while the analysis done by L. H. Weiss et al. (2021) was done on grism-selected 3D-HST galaxies, found principally through emission at [O III] λ5007.

Studies such as those of L. H. Weiss et al. (2021) and D. K. Erb et al. (2016) report a trend similar to the one we found between $f_{\rm esc}^{\rm Ly\alpha}$ and the ionization parameter. The correlation is due to the fact that a harder ionizing radiation field can enhance Lyα production through enhanced recombination and production, since it can increase the ionization of the IGM and CGM, increasing both the chance for Lyα to escape the galaxy and the observability of it.

We investigated the Lyα velocity offset to comprehend its influence on Lyα escape within galaxies' internal mechanics. One of the findings we uncover is that the high equivalent width ($W_{\rm Ly\alpha}$) sources, as also observed by R. Endsley et al. (2022), exhibit lower Lyα velocity offsets, possibly due to reduced H I column densities near systemic velocities, facilitating Lyα escape. This interpretation aligns with findings by

S. L. Finkelstein et al. (2011) and M. Song et al. (2014), where they emphasize low dust and H I as primary factors for Lyα detection. Studies by C. C. Steidel et al. (2010) and D. K. Erb et al. (2016) on LBGs at redshifts 2.2 and 2, respectively, show substantial velocity offsets, yet no direct correlation between $\Delta v_{\mathrm{Ly}\alpha}$ and Lyα escape, suggesting other predominant drivers for Lyα escape in our detected galaxies. Other studies, however, show the opposite trends, such as those of T. Hashimoto et al. (2013), D. K. Erb et al. (2014), and T. Shibuya et al. (2014), who find an anticorrelation between $\Delta v_{\mathrm{Ly}\alpha}$ and Lyα escape. The main difference between our studies is that they include sources with little to no Lyα emission. Given the sensitivity limit of HET, we are not as sensitive to the faint Lyα emitting galaxies. While $\Delta v_{\mathrm{Ly}\alpha}$ can play a role in the escape of Lyα and increase its observability, there is no direct evidence of this being the key factor in leading to its escape in our sample of Lyα-detected galaxies.

6. Summary

We present the results from a comprehensive analysis of galaxies selected from the MOSDEF survey, aiming to unravel the physical disparities between two distinct groups: those with detected Lyα line emission in the HETDEX survey and those without. Our primary objective is to gain deeper insights into the pivotal galaxy properties and ISM conditions that facilitate the escape of Lyα emission. Our investigation reveals the following findings:

1. We find that the Lyα-detected sample exhibits significantly lower stellar mass and SED-derived dust extinction (A_V), both exceeding a 2σ significance. We observe less significant differences, at the 1σ level, suggesting that the ionization parameter is higher, and the metallicity is lower in the Lyα-detected sample. We find no statistically significant differences with sSFR between the two populations.
2. Our analysis reveals moderate correlations between the Lyα escape fraction ($f_{\mathrm{esc}}^{\mathrm{Ly}\alpha}$) and key galaxy properties. $f_{\mathrm{esc}}^{\mathrm{Ly}\alpha}$ exhibits moderate anticorrelations with stellar mass, SFR, and SED-derived dust, all exceeding 2σ. Concurrently, we observe a moderate positive correlation between $f_{\mathrm{esc}}^{\mathrm{Ly}\alpha}$ and the ionization parameter, also exceeding 2σ. These results highlight the critical role played by the ISM conditions and ionizing radiation in facilitating the escape of Lyα radiation from galaxies.
3. The median Lyα velocity offsets for the Lyα-detected sample is approximately 178 km s^{-1}. Our analysis did not reveal any compelling evidence suggesting that this velocity offset plays a pivotal role in the escape of Lyα. However, it is important to note that our sample is limited to galaxies with high $W_{\mathrm{Ly}\alpha}$, which could introduce a potential bias into our results.

Our study demonstrates that several factors contribute to higher $f_{\mathrm{esc}}^{\mathrm{Ly}\alpha}$, including lower stellar mass and lower dust attenuation. These trends with $f_{\mathrm{esc}}^{\mathrm{Ly}\alpha}$ can be degenerate with galaxy properties, as many galaxy properties typically correlate with other galaxy properties, such as SFR and stellar mass, dust and stellar mass, etc. Dust plays a significant role in the destruction of the Lyα emission, thus a system with low dust will reduce the chance of Lyα being destroyed within the galaxy.

Our Lyα-detected galaxies have lower masses than the Lyα-nondetected sample. The lower gravitational potential in lower-mass galaxies provides high-energy phenomena (e.g., supernovae, AGN feedback, and stellar feedback) an easier chance to clear out material, enhancing Lyα escape. The tentative 1σ differences between the two populations between ionization parameter and metallicity also support this interpretation. It has been shown in the literature that metallicity plays a significant role in regulating the ionization parameter, with a lower metallicity resulting in a high ionization parameter (K. Nakajima et al. 2013; D. K. Erb et al. 2016). These two parameters go hand in hand, and these results provide even more evidence that the internal galaxy properties determine the ability of Lyα photons to escape.

While our results, combined with those in the literature, tell an emerging, consistent picture of how Lyα photons escape galaxies, our sample size is modest. While this is a first step in understanding the intricate roles that ISM conditions have on Lyα escape and what properties aid and/or hinder its escape, a comparative analysis with a much larger sample, including reducing biases when possible (e.g., based on continuum or Lyα luminosity) needs to be undertaken to make this claim more robust. Having a large sample with a wide range of dynamic range in all the properties covered here would be the ideal means to study how much each property impacts the escape of Lyα.

Acknowledgments

O.C.O. thanks the University of Texas at Austin, the Dean's Mentoring Fellowship and the NASA FINESST Fellowship for additional support. O.C.O., G.C.K.L., and S.L.F. acknowledge support from the NSF through NSF AAG award 1908817, and NASA through ADAP award 80NSSC22K0489 and the FINESST award 22-ASTRO22-0224.

The observations were obtained with the Hobby–Eberly Telescope (HET), which is a joint project of the University of Texas at Austin, the Pennsylvania State University, Ludwig-Maximilians–Universät München, and Georg-August–Universät Göttingen. The HET is named in honor of its principal benefactors, William P. Hobby and Robert E. Eberly.

VIRUS is a joint project of the University of Texas at Austin, Leibniz-Institut für Astrophysik Potsdam (AIP), Texas A&M University (TAMU), Max-Planck Institut für Extraterrestrische Physik (MPE), Ludwig Maximilians-Universät at München, Pennsylvania State University, Institut für Astrophysik Göttingen, University of Oxford, and the Max-Planck-Institut für Astrophysik (MPA).

The authors acknowledge the Texas Advanced Computing Center (TACC) at The University of Texas at Austin for providing high-performance computing, visualization, and storage resources that have contributed to the research results reported within this paper.

This work is based on observations taken by the 3D-HST Treasury Program (GO 12177 and 12328) with the NASA/ESA HST, which is operated by the Association of Universities for Research in Astronomy, Inc., under NASA contract NAS5-26555.

The Institute for Gravitation and the Cosmos is supported by the Eberly College of Science and the Office of the Senior Vice President for Research at The Pennsylvania State University.

We also want to acknowledge that we did this work at an institution, the University of Texas at Austin, that sits on indigenous land. The Tonkawa live in central Texas and the Comanche and Apache move through this area. We pay respects to all the American Indian and Indigenous Peoples and communities who are a part of these lands and territories in Texas. We are grateful to be able to live, work, collaborate, and learn on this piece of Turtle Island.

Software: Astropy (Astropy Collaboration et al. 2013, 2018, 2022), Numpy (C. R. Harris et al. 2020), Scipy (P. Virtanen et al. 2020), Matplotlib (J. D. Hunter 2007), Astropy (Astropy Collaboration et al. 2013, 2018, 2022), Numpy (C. R. Harris et al. 2020), Pandas (W. McKinney 2010), Scipy (P. Virtanen et al. 2020), Matplotlib (J. D. Hunter 2007).

ORCID iDs

Óscar A. Chávez Ortiz https://orcid.org/0000-0003-2332-5505
Gene C. K. Leung https://orcid.org/0000-0002-9393-6507
Steven L. Finkelstein https://orcid.org/0000-0001-8519-1130
Dustin Davis https://orcid.org/0000-0002-8925-9769
Ralph S. Sutherland https://orcid.org/0000-0002-6620-7421
David C. Nicholls https://orcid.org/0000-0003-0892-5203
Mabel Stephenson https://orcid.org/0000-0003-4717-0376
Erin Mentuch Cooper https://orcid.org/0000-0002-2307-0146
Micaela Bagley https://orcid.org/0000-0002-9921-9218
Karl Gebhardt https://orcid.org/0000-0002-8433-8185
Lindsay R. House https://orcid.org/0000-0002-1496-6514
Chenxu Liu https://orcid.org/0000-0001-5561-2010
Robin Ciardullo https://orcid.org/0000-0002-1328-0211
Caryl Gronwall https://orcid.org/0000-0001-6842-2371
Gary J. Hill https://orcid.org/0000-0001-6717-7685
Daniel Farrow https://orcid.org/0000-0003-2575-0652
Donald P. Schneider https://orcid.org/0000-0001-7240-7449

References

Ahumada, R., Allende Prieto, C., Almeida, A., et al. 2020, ApJS, 249, 3
Amarsi, A. M., Nissen, P. E., Asplund, M., Lind, K., & Barklem, P. S. 2019, A&A, 622, L4
Arellano-Córdova, K. Z., Berg, D. A., Chisholm, J., et al. 2022, ApJL, 940, L23
Astropy Collaboration, Price-Whelan, A. M., Lim, P. L., et al. 2022, ApJ, 935, 167
Astropy Collaboration, Price-Whelan, A. M., Sipőcz, B. M., et al. 2018, AJ, 156, 123
Astropy Collaboration, Robitaille, T. P., Tollerud, E. J., et al. 2013, A&A, 558, A33
Atek, H., Kunth, D., Hayes, M., Östlin, G., & Mas-Hesse, J. M. 2008, A&A, 488, 491
Atek, H., Kunth, D., Schaerer, D., et al. 2009, A&A, 506, L1
Backhaus, B. E., Trump, J. R., Pirzkal, N., et al. 2024, ApJ, 962, 195
Bassett, R., Ryan-Weber, E. V., Cooke, J., et al. 2019, MNRAS, 483, 5223
Bian, F., Kewley, L. J., & Dopita, M. A. 2018, ApJ, 859, 175
Bourne, N., Maddox, S. J., Dunne, L., et al. 2012, MNRAS, 421, 3027
Brammer, G. B., van Dokkum, P. G., Franx, M., et al. 2012, ApJS, 200, 13
Brinchmann, J., Charlot, S., White, S. D. M., et al. 2004, MNRAS, 351, 1151
Brown, J. S., Martini, P., & Andrews, B. H. 2016, MNRAS, 458, 1529
Bruzual, G., & Charlot, S. 2003, MNRAS, 344, 1000
Calzetti, D., Armus, L., Bohlin, R. C., et al. 2000, ApJ, 533, 682
Carnall, A. C., McLure, R. J., Dunlop, J. S., & Davé, R. 2018, MNRAS, 480, 4379
Carnall, A. C., McLure, R. J., Dunlop, J. S., et al. 2019, MNRAS, 490, 417
Chavez Ortiz, O. A., Finkelstein, S. L., Davis, D., et al. 2023, ApJ, 952, 110
Chen, Z., Stark, D. P., Mason, C., et al. 2024, MNRAS, 528, 7052
Chevallard, J., & Charlot, S. 2016, MNRAS, 462, 1415
Cowie, L. L., Barger, A. J., & Songaila, A. 2016, ApJ, 817, 57
Cullen, F., Shapley, A. E., McLure, R. J., et al. 2021, MNRAS, 505, 903
Davis, D., Gebhardt, K., Cooper, E. M., et al. 2023a, ApJ, 946, 86
Davis, D., Gebhardt, K., Cooper, E. M., et al. 2023b, ApJ, 954, 209
Del Zanna, G., Dere, K. P., Young, P. R., Landi, E., & Mason, H. E. 2015, A&A, 582, A56
Dere, K. P., Landi, E., Mason, H. E., Monsignori Fossi, B. C., & Young, P. R. 1997, A&AS, 125, 149
Dijkstra, M. 2014, PASA, 31, e040
Dijkstra, M., Gronke, M., & Venkatesan, A. 2016, ApJ, 828, 71
Domínguez, A., Siana, B., Henry, A. L., et al. 2013, ApJ, 763, 145
Du, X., Shapley, A. E., Topping, M. W., et al. 2021, ApJ, 920, 95
Endsley, R., Stark, D. P., Bouwens, R. J., et al. 2022, MNRAS, 517, 5642
Erb, D. K., Pettini, M., Steidel, C. C., et al. 2016, ApJ, 830, 52
Erb, D. K., Shapley, A. E., Pettini, M., et al. 2006, ApJ, 644, 813
Erb, D. K., Steidel, C. C., Trainor, R. F., et al. 2014, ApJ, 795, 33
Fan, X., Strauss, M. A., Becker, R. H., et al. 2006, AJ, 132, 117
Farrow, D. J., Sánchez, A. G., Ciardullo, R., et al. 2021, MNRAS, 507, 3187
Ferland 2017, The 2017 Release Cloudy, v17.02, Zenodo, doi:10.5281/zenodo.4110791
Fetherolf, T., Reddy, N. A., Shapley, A. E., et al. 2021, MNRAS, 508, 1431
Finkelstein, S., Bradac, M., Casey, C., et al. 2019, BAAS, 51, 221
Finkelstein, S. L., D’Aloisio, A., Paardekooper, J.-P., et al. 2019, ApJ, 879, 36
Finkelstein, S. L., Hill, G. J., Gebhardt, K., et al. 2011, ApJ, 729, 140
Finkelstein, S. L., Rhoads, J. E., Malhotra, S., & Grogin, N. 2009, ApJ, 691, 465
Froese Fischer, C., & Tachiev, G. 2004, ADNDT, 87, 1
Gebhardt, K., Mentuch Cooper, E., Ciardullo, R., et al. 2021, ApJ, 923, 217
Grogin, N. A., Kocevski, D. D., Faber, S. M., et al. 2011, ApJS, 197, 35
Gronwall, C., Ciardullo, R., Hickey, T., et al. 2007, ApJ, 667, 79
Groves, B., Dopita, M. A., Sutherland, R. S., et al. 2008, ApJS, 176, 438
Guaita, L., Acquaviva, V., Padilla, N., et al. 2011, ApJ, 733, 114
Gunn, J. E., & Peterson, B. A. 1965, ApJ, 142, 1633
Harris, C. R., Millman, K. J., van der Walt, S. J., et al. 2020, Natur, 585, 357
Hashimoto, T., Ouchi, M., Shimasaku, K., et al. 2013, ApJ, 765, 70
Hayes, M., Schaerer, D., Östlin, G., et al. 2011, ApJ, 730, 8
Hill, G. J., Lee, H., MacQueen, P. J., et al. 2021, AJ, 162, 298
Hunter, J. D. 2007, CSE, 9, 90
Kauffmann, G., Heckman, T. M., Tremonti, C., et al. 2003, MNRAS, 346, 1055
Kennicutt, R. C., Jr., & Evans, N. J., II 2012, ARA&A, 50, 531
Kennicutt, R. C., Jr. 1992, ApJ, 388, 310
Kennicutt, R. C., Jr. 1998, ARA&A, 36, 189
Kewley, L. J., & Ellison, S. L. 2008, ApJ, 681, 1183
Kewley, L. J., Groves, B., Kauffmann, G., & Heckman, T. 2006, MNRAS, 372, 961
Kewley, L. J., Maier, C., Yabe, K., et al. 2013, ApJL, 774, L10
Kewley, L. J., Nicholls, D. C., Sutherland, R., et al. 2019, ApJ, 880, 16
Kisielius, R., Storey, P. J., Ferland, G. J., & Keenan, F. P. 2009, MNRAS, 397, 903
Koekemoer, A. M., Faber, S. M., Ferguson, H. C., et al. 2011, ApJS, 197, 36
Kornei, K. A., Shapley, A. E., Erb, D. K., et al. 2010, ApJ, 711, 693
Kriek, M., Shapley, A. E., Reddy, N. A., et al. 2015, ApJS, 218, 15
Kroupa, P. 2001, MNRAS, 322, 231
Kumari, N., Amorín, R., Pérez-Montero, E., Vílchez, J., & Maiolino, R. 2021, MNRAS, 508, 1084
Langeroodi, D., Hjorth, J., Chen, W., et al. 2023, ApJ, 957, 39
Laseter, I. H., Maseda, M. V., Curti, M., et al. 2024, A&A, 681, A70
Laursen, P., Sommer-Larsen, J., & Andersen, A. C. 2009, ApJ, 704, 1640
Leitherer, C., Schaerer, D., Goldader, J. D., et al. 1999, ApJS, 123, 3
Leung, A. S., Acquaviva, V., Gawiser, E., et al. 2017, ApJ, 843, 130
Leung, G. C. K., Coil, A. L., Aird, J., et al. 2019, ApJ, 886, 11
Liu, C., Gebhardt, K., Cooper, E. M., et al. 2022, ApJS, 261, 24
Luridiana, V., Morisset, C., & Shaw, R. A. 2015, A&A, 573, A42
Malhotra, S., & Rhoads, J. E. 2006, ApJL, 647, L95
Matthee, J., Sobral, D., Oteo, I., et al. 2016, MNRAS, 458, 449
McCarron, A. P., Finkelstein, S. L., Chavez Ortiz, O. A., et al. 2022, ApJ, 936, 131
McKinney, W. 2010, in Proc. 9th Python in Science Conf., ed. S. van der Walt & J. Millman, 61
McLean, I. S., Steidel, C. C., Epps, H. W., et al. 2012, Proc. SPIE, 8446, 84460J
Mentuch Cooper, E., Gebhardt, K., Davis, D., et al. 2023, ApJ, 943, 177
Miralda-Escudé, J. 1998, ApJ, 501, 15
Momcheva, I. G., Brammer, G. B., van Dokkum, P. G., et al. 2016, ApJS, 225, 27
Nakajima, K., & Ouchi, M. 2014, MNRAS, 442, 900

Nakajima, K., Ouchi, M., Isobe, Y., et al. 2023, ApJS, 269, 33
Nakajima, K., Ouchi, M., Shimasaku, K., et al. 2013, ApJ, 769, 3
Napolitano, L., Pentericci, L., Santini, P., et al. 2024, A&A, 688, A106
Nicholls, D. C., Sutherland, R. S., Dopita, M. A., Kewley, L. J., & Groves, B. A. 2017, MNRAS, 466, 4403
Oke, J. B. 1974, ApJS, 27, 21
Oke, J. B., & Gunn, J. E. 1983, ApJ, 266, 713
Ouchi, M., Ono, Y., & Shibuya, T. 2020, ARA&A, 58, 617
Pahl, A. J., Shapley, A., Steidel, C. C., et al. 2023, MNRAS, 521, 3247
Pengelly, R. M. 1964, MNRAS, 127, 145
Pucha, R., Reddy, N. A., Dey, A., et al. 2022, AJ, 164, 159
Ramsey, L. W., Adams, M. T., Barnes, T. G., et al. 1998, Proc. SPIE, 3352, 34
Reddy, N. A., Kriek, M., Shapley, A. E., et al. 2015, ApJ, 806, 259
Reddy, N. A., Shapley, A. E., Kriek, M., et al. 2020, ApJ, 902, 123
Reddy, N. A., Steidel, C. C., Pettini, M., Bogosavljević, M., & Shapley, A. E. 2016, ApJ, 828, 108
Robertson, B. E., Ellis, R. S., Furlanetto, S. R., & Dunlop, J. S. 2015, ApJL, 802, L19
Rodríguez-Muñoz, L., Rodighiero, G., Pérez-González, P. G., et al. 2022, MNRAS, 510, 2061
Salpeter, E. E. 1955, ApJ, 121, 161
Sanders, R. L., Shapley, A. E., Jones, T., et al. 2021, ApJ, 914, 19
Sanders, R. L., Shapley, A. E., Kriek, M., et al. 2016, ApJ, 816, 23
Sanders, R. L., Shapley, A. E., Reddy, N. A., et al. 2020, MNRAS, 491, 1427
Santini, P., Maiolino, R., Magnelli, B., et al. 2014, A&A, 562, A30
Shapley, A. E., Sanders, R. L., Reddy, N. A., Topping, M. W., & Brammer, G. B. 2023, ApJ, 954, 157
Shapley, A. E., Steidel, C. C., Pettini, M., & Adelberger, K. L. 2003, ApJ, 588, 65
Shibuya, T., Ouchi, M., Nakajima, K., et al. 2014, ApJ, 788, 74
Skelton, R. E., Whitaker, K. E., Momcheva, I. G., et al. 2014, ApJS, 214, 24
Smith, A., Kannan, R., Tacchella, S., et al. 2022, MNRAS, 517, 1
Sobral, D., & Matthee, J. 2019, A&A, 623, A157
Song, M., Finkelstein, S. L., Gebhardt, K., et al. 2014, ApJ, 791, 3
Steidel, C. C., Erb, D. K., Shapley, A. E., et al. 2010, ApJ, 717, 289
Steidel, C. C., Strom, A. L., Pettini, M., et al. 2016, ApJ, 826, 159
Storey, P. J., & Hummer, D. G. 1995, MNRAS, 272, 41
Strom, A. L., Steidel, C. C., Rudie, G. C., et al. 2017, ApJ, 836, 164
Sutherland, R. S., & Dopita, M. A. 2017, ApJS, 229, 34
Topping, M. W., Shapley, A. E., Reddy, N. A., et al. 2020, MNRAS, 495, 4430
Trainor, R. F., Strom, A. L., Steidel, C. C., & Rudie, G. C. 2016, ApJ, 832, 171
Trump, J. R., Arrabal Haro, P., Simons, R. C., et al. 2023, ApJ, 945, 35
Verhamme, A., Schaerer, D., Atek, H., & Tapken, C. 2008, A&A, 491, 89
Verhamme, A., Schaerer, D., & Maselli, A. 2006, A&A, 460, 397
Virtanen, P., Gommers, R., Oliphant, T. E., et al. 2020, NatMe, 17, 261
Weiss, L. H., Bowman, W. P., Ciardullo, R., et al. 2021, ApJ, 912, 100
Whitaker, K. E., Pope, A., Cybulski, R., et al. 2017, ApJ, 850, 208
Wild, V., Charlot, S., Brinchmann, J., et al. 2011, MNRAS, 417, 1760
Yajima, H., Li, Y., Zhu, Q., et al. 2012, ApJ, 754, 118
Yajima, H., Li, Y., Zhu, Q., et al. 2014, MNRAS, 440, 776